nature communications

Article

https://doi.org/10.1038/s41467-025-63530-y

Sustainable eco-friendly printing of high-performance large-area organic photovoltaics via enhanced Laplace pressure gradient

Received: 25 February 2025

Accepted: 21 August 2025

Published online: 26 September 2025

Check for updates

Siqi Liu[1,8], Hanlin Wang[2,8], Yongting Cui[2], Shumin Zeng[2], Chunlong Sun[3], Haojie Li[2], Hongxiang Li[4], Long Ye[3], Hao Yuan[5], Haiming Zhu[6], Jinyang Yu[7], Hongzheng Chen[7], Xiaotian Hu[2,5] ✉ & Yiwang Chen[1,2,5] ✉

The coffee-ring effect during the green-printed process remains a significant bottleneck hindering the scalable fabrication and practical deployment of organic photovoltaics. Here, a fluorinated rheology modifier 1H,1H,10H,10H-Perfluoro-1,10-decanediol is brought to fine-tune the rheological properties of the active layer solution and the shape of the printed gas/liquid confined zone. The Laplace pressure gradient generated by the rheology modifier along printing direction effectively suppresses the coffee-ring effect. This results in enabling the formation of highly uniform large-area active layer films. The gas/liquid confined zone is qualitatively and quantitatively analyzed to understand the function of the Laplace pressure gradient. Meanwhile, the clear fiber network active layer morphology with high crystallinity and moderate phase separation is obtained through the rheology modifier modulation of printing fluid dynamics. Therefore, based on PM6:BTP-eC9:L8-BO (o-xylene), small-area (0.04 cm^2) devices achieve a power conversion efficiency of 20.49%. More importantly, scalable module (16.94 cm^2) harvests a high efficiency of 17.85% with a nice efficiency retention rate of 87.1%. This study broadens the processing window and the range of potential applications for high-throughput green printing of large-area organic photovoltaics.

Organic solar cells (OSCs) hold unique promise for applications in self-powered wearable electronics and building-integrated photovoltaics, owing to their lightweight, compatibility with roll-to-roll manufacturing processes, and ease of integration[1–7]. Currently, following the accelerated advancement of Y-series molecules and device techniques, the power conversion efficiency (PCE) of small-area chloroform-based OSCs has surpassed 20%, which is acceptable to meet the requirements for commercialization[4,8–12]. However, when scaling up from mm-

[1]College of Chemistry and Materials/Key Laboratory of Fluorine and Silicon for Energy Materials and Chemistry of Ministry of Education, Jiangxi Normal University, Nanchang, China. [2]College of Chemistry and Chemical Engineering/Film Energy Chemistry for Jiangxi Provincial Key Laboratory (FEC), Nanchang University, Nanchang, China. [3]School of Materials Science and Engineering, Tianjin University, Tianjin, China. [4]College of Polymer Science and Engineering, State Key Laboratory of Polymer Materials Engineering, Sichuan University, Chengdu, China. [5]Peking University Yangtze Delta Institute of Optoelectronics, Nantong, China. [6]Department of Chemistry, Zhejiang University, Hangzhou, China. [7]State Key Laboratory of Silicon and Advanced Semiconductor Materials/Department of Polymer Science and Engineering, Zhejiang University, Hangzhou, China. [8]These authors contributed equally: Siqi Liu, Hanlin Wang. ✉e-mail: happyhu@ncu.edu.cn; ywchen@ncu.edu.cn

sized laboratory devices to cm-sized modules, the macroscopic uniformity of printed large-area active layer films significantly deteriorates, and precise control over the microstructure becomes increasingly challenging[13–16]. Then, the performance of most modules always lags observably behind that of small-area devices[13,17,18]. Thus, bridging the performance gap that arises as organic photovoltaic devices scale up is a crucial challenge for their industrial advancement.

To facilitate the commercialization of organic photovoltaics, environmentally friendly green solvent printing treatment processes have been developed[17,19]. By contrast to halogenated solvents such as chlorobenzene and chloroform, most green solvents such as toluene and o-xylene (o-XY) usually have higher boiling points and poorer solubility of organic photovoltaic materials[15,20–23]. Therefore, the fluid behavior and the self-aggregation of donor/acceptor are usually disordered for green solvent-treated active layer solution during the printing process[19,22,23]. This hinders the realization of high-performance, uniform active layer films and devices. High-temperature treatment processes[19,21,23], such as hot solution and hot substrate methods, along with vacuum-assisted thermal annealing[24] or assisted electric field techniques[25], have been successfully employed to achieve the active layer films with desirable nanomorphology. These methods facilitate moderate phase aggregation, controlled phase separation and high phase purity, essential for enhancing the performance of the films and devices. However, the research on microscopic modulation of fluid motion to reduce the performance gap between small and scaled devices is still relatively limited.

To achieve highly uniform thin films, the fluid dynamics during the printing process should be finely engineered and controlled to enable high-throughput production of large-area films. The blade-coating process, which is widely used in the field of organic photovoltaic, has the advantages of good device reproducibility and high film homogeneity[17,26–28]. And it applies a unidirectional shearing force to spread the solution into a homogeneous wet film through the relative motion of the fixed gap between the blade and the substrate, followed by solvent evaporation to form the final dry film[28,29]. Accordingly, the fluid dynamics during the printing process play a crucial role in the formation of the films. And importantly, the rheological properties of the solution, including viscosity and surface tension, significantly influence the phase separation and crystallization behavior of the final active layer film[14,29–31]. During the blade-coating process, the evaporation rate of the solvent at the edge of the three-phase contact line is higher than that in the bulk solution, inducing a capillary force-driven compensatory flow towards the edge[32,33]. This capillary flow leads to solute deposition and pinning at the periphery, resulting in an uneven film at nano/micro scales with significant aggregation, a phenomenon known as the coffee ring effect (CRE)[34]. In this instance, larger polymer molecules are driven inward by the internal forces at the wedge-shaped edge of the three-phase contact line, leading to their preferential distribution in the interior. In contrast, smaller molecules tend to accumulate at the edge of three-phase contact line on account of capillary flow[35]. To enhance the uniformity and get controlled thickness of the printed films, Marangoni flow and Laplace pressure gradient, which is related to surface tension, are often established to homogenize solute deposition[32,36–38].

The introduction of rheological modifiers, such as cosolvent or surfactants, can establish inward Marangoni flows to suppress capillary force-induced CRE, which indirectly achieve more even solute deposition[28,39]. Similarly, Laplace pressure gradient within solution that arises from surface tension at the curved interface is influenced by the addition of rheology modifiers. Unlike Marangoni flows, which regulate capillary flows, a moderately increased Laplace pressure gradient directly opposes the movement and deposition of particles at the edges from the force perspective[38,40,41]. This modulation directly promotes the even distribution of solutes during printing[37,39]. More concretely, the regulation of the Laplace pressure gradient within the gas/liquid confined zone is beneficial to promote uniform spreading over a larger area and eliminate the effect of surface defects in the interfacial layer. In addition, optimization the Laplace pressure gradient at the three-phase contact line can control the rate of solvent evaporation during printing, which is conducive to reducing the film defects such as pinholes and excessive solute aggregation caused by rapid local evaporation[38,40,42,43]. Therefore, high-quality large-area active layer films can be obtained by carefully modulating Laplace pressure gradient within solution through the use of suitable rheology modifiers.

Common rheology modifiers, predominantly surfactants, could modulate the curvature of gas/liquid confined interface by reducing solution surface tension and regulating viscosity during printing[44–46]. Classified by ionization behavior, these include ionic, non-ionic, and amphoteric ionic types (Supplementary Fig. 1 and Supplementary Table 1). To regulate the wet film spreading rheological behavior of the active layer solution during blade-coating, an effective modifier should have a lower surface tension than the processing solvent[46,47]. Moreover, to enable precise characterization of rheological mechanisms, the dried film must be devoid of residual rheology modifiers or associated ions while preserving the active layer's internal morphology from being destroyed[48]. Accordingly, ionic or amphoteric rheology modifiers are not selected. Also, polymeric modifiers are unsuitable, as their large size hinders diffusion and complicates their complete removal[49]. Consequently, low-surface-tension, non-ionic, small-molecule rheology modifiers are selected for modulating the active layer solution. Furthermore, general requirements for the rheology modifiers also should be fulfilled, such as the stability and safety of the material itself in the process environment.

In this work, we incorporate a non-ionic fluorinated small-molecule rheology modifier, 1H,1H,10H,10H-Perfluoro-1,10-decanediol (FDDO), into the active layer solution to enable the printing of high-quality large-area films. The FDDO meeting selection principle of rheology modifier can significantly enhance the rheological behavior of the gas/liquid confined zone especially at three-phase contact lines, improving the wettability, the interfacial curvature and the solvent evaporation rate during the blade-coating process. The addition of FDDO in the solution enhances the Laplace pressure gradient along the printing direction. The enhanced Laplace pressure gradient counteracts the capillary force, reducing the movement of small molecules toward the three-phase contact line. Thus, the CRE caused by edge capillary flow is suppressed. Meanwhile, due to changes in wetting property and contact angle at the three-phase contact line, the increase in vertical component force is conducive to the crystallization of polymers. The disordered aggregation and distribution of internal molecules are mitigated, thereby eliminating inhomogeneity in the active layer film during area expansion. Consequently, the PM6:BTP-eC9 binary system optimized by FDDO exhibits a high module PCE of 16.55% and a good PCE retention rate of 88.7% as the active area scaled up from 0.04 cm^2 to 16.94 cm^2. Besides, the photostability and damp-heat stability of the devices are significantly improved. Furthermore, FDDO exhibits broad compatibility with diverse active layer solutions due to its inertness toward photovoltaic materials in the active layer and complete ethanol elution. The PM6:BTP-eC9:L8-BO ternary system is successfully utilized for the universal validation. The advanced PCE and the corresponding PCE retention for the modules are 17.85% and 87.1%, respectively. In summary, this strategy is applicable to the scalable printing of organic photovoltaics.

Results

The chemical structures of the non-halogenated solvent (o-XY), the rheology modifier (FDDO) and the organic photovoltaic materials (PM6[50], BTP-eC9[51] and L8-BO[52]) are shown in Fig. 1a. The non-ionic small molecule rheology modifier FDDO has a lower surface tension (18.9 mN m^{-1}) than the processing solvent o-XY (28.7 mN m^{-1}). And the

https://doi.org/10.1038/s41467-025-63530-y

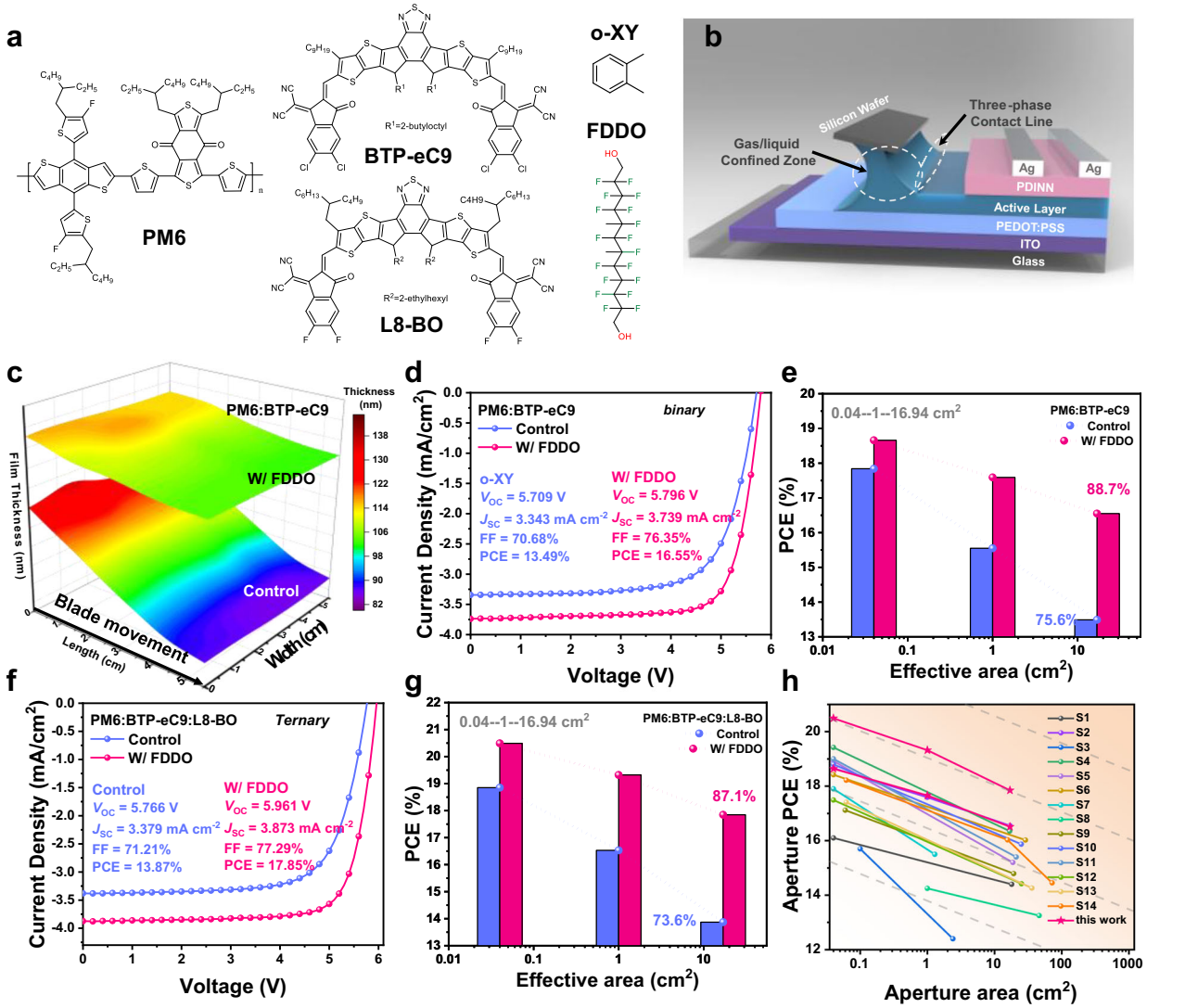

Fig. 1 | Materials, photoelectric properties of green-printed devices. a Chemical structures of PM6, BTP-eC9, L8-BO, FDDO and o-XY. **b** Schematic illustration of the devices structure. **c** Thickness distribution of large-area (5 cm × 5 cm) printed active layer films based on PM6:BTP-eC9 without and with FDDO, where the blade moves from length 0 cm to length 5 cm. **d** *J*–*V* characteristics of OSCs based on PM6:BTP-eC9 binary system without/with FDDO. **e** PCE versus area of the OSCs based on PM6:BTP-eC9 binary system without/with FDDO. **f** *J*–*V* characteristics of OSCs based on PM6:BTP-eC9:L8-BO ternary system without/with FDDO. **g** PCE versus area of the OSCs based on PM6:BTP-eC9:L8-BO ternary system without/with FDDO. **h** Summary of PCE versus area of the active layer for the green-printed OSCs in other literature and in the present work. Source data are provided as a Source Data file.

thermal decomposition temperature of FDDO is 130 °C at 5% degradation, ensuring stable operation at high printing temperature (approaching 100 °C), as displayed in Supplementary Fig. 2. Also, the ethanol solubility of FDDO is up to about 3 g/ml, which facilitates subsequent alcohol elution for removing operations (Supplementary Fig. 3). Thus, FDDO exhibits a combination of good rheological properties, nice thermal stability at experimental temperatures, and facile removal characteristics, which match the printing of the active layer. More significantly, a comprehensive description of the advantages of FDDO among various rheology modifiers based on rheology modifiers' selection principle and deeper device tests is provided in Supplementary Note I. The diagram of the device structure (ITO/PEDOT:PSS/Active layer/PDINN/Ag) employed in this study is illustrated in Fig. 1b, with an emphasis on the modulation of the printed gas/liquid confined zone especially at three-phase contact lines. Herein, bringing in FDDO primarily homogenizes the distribution of donor/acceptor through fluidic fine-tuning during blade-coating process, thereby preventing inhomogeneous deposition in large-area (25 cm^2) active layer films. And the films, both un- and FDDO-optimized, are prepared by using hot blade-coating process. The corresponding digital images are shown in Supplementary Fig. 4. The un-optimized active layer film displays pronounced vertical striations and numerous, albeit lighter, horizontal striations. These features primarily arise from the CRE and stick-slip phenomena, induced by disordered fluid dynamics during the thermal printing process. The movement of small molecules in the solution toward the three-phase line due to capillary flow is the main cause of the CRE. In contrast, the optimized film exhibits a continuous, defect-free homogeneous morphology. Afterwards, to further illustrate the positive impact of the rheological regulation strategy on high-quality large-area film formation, the thickness distribution and optical microscopy (OM) images and surface profile lines of the corresponding films are presented in Fig. 1c and Supplementary Fig. 5. The thickness of the o-XY-based active layer film varies from 128 nm to 86 nm along the blade-coating direction, with a difference of 42 nm. Conversely, the o-XY:FDDO-based film displays a more uniform thickness variation, ranging from 117 nm to 103 nm, with a difference of only 14 nm. Additionally, optical microscopy images of the optimized active layer films exhibit a more uniform morphology with the

Table 1 | Photovoltaic parameters of OSC modules under different conditions under simulated solar illumination (AM 1.5 G, 100 mW/cm^2)

System	Processing method	V_{OC} (V)	J_{SC} (mA/cm^2)	FF (%)	PCE_{max} (PCE[a]) (%)	PCE ret. rate[b] (%)
PM6:BTP-eC9	Control	5.71	3.34	70.7	13.49 (12.81 ± 0.61)	75.6
	W/ FDDO	5.80	3.74	76.4	16.55 (15.82 ± 0.56)	88.7
PM6:BTP-eC9:L8-BO	Control	5.77	3.38	71.2	13.87 (13.12 ± 0.63)	73.6
	W/ FDDO	5.96	3.87	77.3	17.85 (17.21 ± 0.54)	87.1

[a]The average PCEs are obtained from 6 independent modules.
[b]The PCE ret. rate reflects the retention of PCE in large-area (16.94 cm^2) modules when the device area is extended from 0.04 cm^2 to 16.94 cm^2.

slighter coffee ring effect pattern, compared to the control samples (Supplementary Fig. 5a). More deeply, the surface profile scanning of the OM images is carried out to quantitatively evaluate morphological homogeneity (Supplementary Fig. 5b). The dark and bright areas in the OM images represent high and low thickness states of films, respectively. The FDDO-optimized film exhibits smoother profile fluctuations (~4 nm) compared to the control (~11 nm) film, consistent with the results of the OM images. Besides, to further display the manifestation of CRE on film-forming homogeneity, three-dimensional (3D) microscopy images of the active layer films without/with FDDO optimization are recorded, and the extracted two-dimensional (2D) images and one-dimensional (1D) profile lines are analyzed (Supplementary Fig. 6). The optimized samples exhibited a smoother, streak-free uniform morphology than the control samples, verifying the results of the OM test (Supplementary Fig. 6a). Meanwhile, the fluctuation of the 2D image and 1D contour lines of FDDO-optimized sample is smaller than the control sample both in the horizontal and vertical directions, revealing the inhibition effect of FDDO on CRE (Supplementary Fig. 6b–g). Based on above results, FDDO can significantly enhance the macroscopic uniformity of large-area active layer films during printing, mitigating morphological discrepancies as the film area increases.

To investigate the relationship between morphological variations and device performance across different film areas, the devices and modules based on PM6:BTP-eC9 binary system with varying active areas are fabricated, as shown in Fig. 1d, e. And the corresponding photograph of the scalable large-area devices and modules is displayed in Supplementary Figs. 7 and 8. First, Supplementary Figs. 9–13 and Supplementary Tables 2–6 present the photovoltaic performance of small-area (0.04 cm^2) OSCs based on the PM6:BTP-eC9 system fabricated by using the green blade-printing process. During these series of blade-coating parameters exploration experiments of OSCs, the optimal content of FDDO is first established as 3 wt% (optimal weight percentage according to photovoltaic materials). Afterwards, to obtain better photovoltaic performance, various blade-coating parameters are systematically investigated based on the active layer solution with FDDO (3 wt%). Among them, the optimal substrate temperature, blade speed and blade-substrate angle are established to be 95 °C, 45 mm s^{-1} and 25°, respectively. And the detailed and systematic description of exploration processes of blade-coated printing process parameters for PM6:BTP-eC9-based devices is provided in Supplementary Note II. Ultimately, the device without FDDO treatment exhibits a PCE of 17.84%, with a short-circuit current density (J_{SC}) of 26.78 mA/cm^2, an open-circuit voltage (V_{OC}) of 0.854 V, and a fill factor (FF) of 78.1%. Comparatively, the performance of OSCs optimized with FDDO (3 wt%) is significantly enhanced, achieving a high PCE of 18.66%, a J_{SC} of 27.53 mA/cm^2, and an FF of 79.4%. Additionally, the external quantum efficiency (EQE) response is enhanced in both the PM6 (350-500 nm) and BTP-eC9 (830-900 nm) absorption regions for the FDDO-optimized devices, consistent with the *J-V* characteristics.

While the improvement in the performance of small-area OSCs is favorable, it is even more crucial to minimize performance gap when expanding the device area. Figure 1d, e and Supplementary Figs. 14, 15 demonstrate the *J–V* curves and the corresponding retention rates of PCE of the scalable OSCs (active areas of 1, 1.44, 3, 4 and 16.94 cm^2, respectively) based on PM6:BTP-eC9 system. And the corresponding photovoltaic parameters of the modules are summarized in Table 1 and Supplementary Table 7, 8. In PM6:BTP-eC9 system, the optimal module (16.94 cm^2) exhibits higher performance with a PCE of 16.55%, a J_{SC} of 3.739 mA/cm^2, a V_{OC} of 5.796 V and an FF of 76.4% than the control sample with a PCE of 13.49%, a J_{SC} of 3.343 mA/cm^2, a V_{OC} of 5.709 V and an FF of 70.7% (Fig. 1d). More deeply, upon increasing the active area of devices from 0.04 cm^2 to 16.94 cm^2, the PCE of the control samples decrease from 17.84% to 13.49%, corresponding to a PCE retention of 75.6%. And the FDDO-optimized OSCs exhibit a PCE reduction from 18.66% (0.04 cm^2) to 16.55% (25 cm^2), achieving an advanced PCE retention of 88.7% (Fig. 1e, Supplementary Table 7-8 and Table 1). Besides, as device area scales continuously, the degradation of the photoelectric performance of the devices slows down after FDDO optimization (Supplementary Fig. 15). The good module performance is attributed to the low J_{SC} loss and FF loss, primarily due to the effective control of the active layer film morphology upon area expanding.

To elucidate the advantages of FDDO rheology modifier, two alternative modifiers Carvone and Dimethylsiloxane are systematically evaluated. These modifiers meeting the rheology modifier selection principle, and the corresponding devices are fabricated under different active areas (0.04 cm^2 and 1 cm^2) (Supplementary Figs. 16, 17 and Supplementary Tables 9 and 10). The corresponding PCE retention rates are calculated and summarized in Supplementary Fig. 18. In small-area (0.04 cm^2) devices, the performance of the Carvone-based devices (PCE of 15.88%, a J_{SC} of 25.82 mA/cm^2 and an FF of 73.5%) lagged behind the control devices (PCE of 17.84%, a J_{SC} of 26.78 mA/cm^2 and an FF of 78.1%), potentially resulting from the lower flash point characteristic mismatching the high-temperature blade-coating process (Supplementary Fig. 16). Whereas, the Dimethylsiloxane-based devices have exceedingly poor performance than the control devices. The challenging removal of Dimethylsiloxane compromises film morphology and device performance, as evidenced by the observed Ag surface roughness (Supplementary Fig. 17). More significantly, the large-area (1 cm^2) FDDO-based devices exhibits the best performance (PCE of 17.84%) and high PCE retention (94.3%) compared to the Carvone-based (PCE of 13.32% and PCE retention of 83.9%) and Dimethylsiloxane-based (exceedingly poor PCE of 0.354%) devices, demonstrating the advantages of FDDO as a suitable rheology modifier. And the more profound expression is presented in Supplementary Note I. Furthermore, to thoroughly assess the universality of FDDO in green solvents, the performance of devices treated with Toluene (Tol) and Carbon disulfide (CS_2) based on the PM6:BTP-eC9 system are carried out, respectively (Supplementary Figs. 19, 20 and Supplementary Tables 11, 12). The same performance decreasing pattern is kept (Supplementary Fig. 21). In small-area (0.04 cm^2) devices, the PCEs of both Tol-treated devices (18.24%) and CS_2-treated devices (14.38%) are improved after FDDO optimization, better than the performance of the corresponding control (17.48% for Tol-based devices and 12.21% for CS_2-based devices, respectively). While in large-area (1 cm^2) devices, the PCE retention of the FDDO-optimized Tol-treated devices (93.1%) and CS_2-treated devices (88.6%) is increased compared to the control devices (86.5% for Tol-based devices and 77.6% for

https://doi.org/10.1038/s41467-025-63530-y

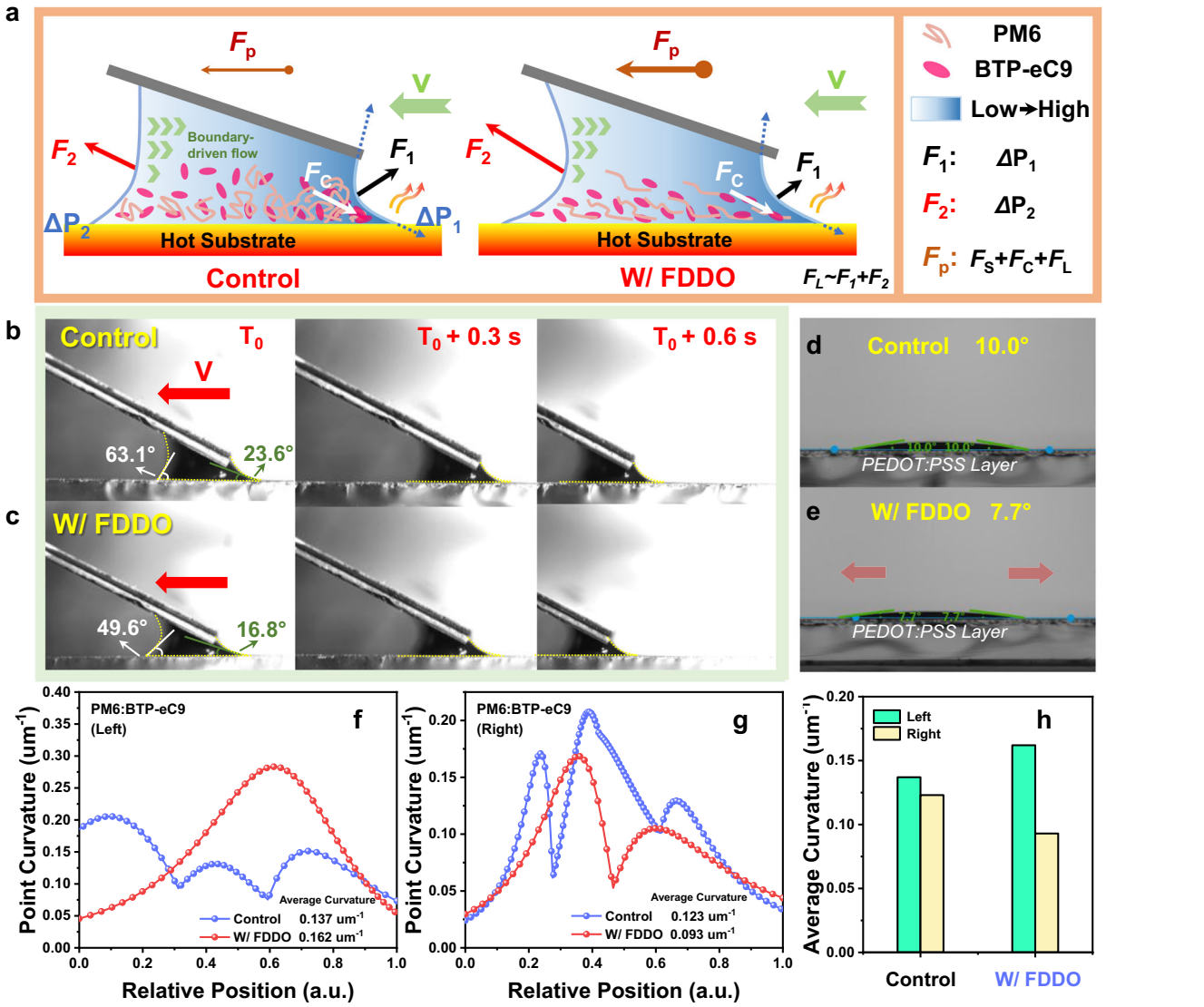

Fig. 2 | Regulation and analysis of fluid mechanics behavior of blade-coating process. a Summary of forces, gradients, and fluid mechanical phenomena during the blade process based on o-XY and o-XY:FDDO solvents, showing the discrepancy between the shapes of the left and right three-phase interfaces. **b**, **c** Photographs of gas/liquid confined zones based on high-speed camera recordings of printed large-area (5 cm × 5 cm) active layer films based on PM6:BTP-eC9 without/with FDDO at different times. **d**, **e** Contact angle of PM6:BTP-eC9-based active layer solution on PEDOT:PSS substrate without/with FDDO. **f** Curvature variation of the left interface in printed gas/liquid confined zone. **g** Curvature variation of the right (evaporated) interface in printed gas/liquid confined zone. **h** Summary of the mean curvature of the interfaces in printed gas/liquid confined zone. Source data are provided as a Source Data file.

CS_2-based devices, respectively). To thoroughly explore the generality of FDDO in multiple active layer systems with different aggregation dynamics, corresponding performance validations of the devices based on PTQ10:BTP-eC9 and PM6:IT-4F systems are analyzed, respectively (Supplementary Figs. 22, 23 and Supplementary Tables 13, 14). The results indicate that appropriate FDDO doping can improve the performance of small-area devices while eliminating performance discrepancies that arise as the device area scales up. A more specific description is placed in Supplementary Note III. Also, the PM6:BTP-eC9:L8-BO ternary system is used to verify the universal validity of the pattern (Fig. 1f-g). When the active layer system is extended to ternary blend film based on PM6:BTP-eC9:L8-BO, the same regularity is maintained in the ternary scalable OSCs (Supplementary Figs. 24, 25 and Supplementary Table 15). Following FDDO modulation, the small-area (0.04 cm^2) ternary devices obtain a PCE of up to 20.49% with a J_{SC} of 28.75 mA/cm^2, a V_{OC} of 0.873 V and an FF of 81.7%, which is one of the highest PCEs for green-printed OSCs devices so far, in comparison to the low PCE (18.85% with a J_{SC} of 27.34 mA/cm^2, a V_{OC} of 0.874 V and an FF of 78.9%) of the control devices. More importantly, the FDDO-optimized ternary modules still achieve a high module efficiency of 17.85% (with a J_{SC} of 3.873 mA/cm^2, a V_{OC} of 5.961 V and an FF of 77.3%) and maintain nice PCE retention (87.1%), in contrast to the inferior module performance (13.87% with a J_{SC} of 3.379 mA/cm^2, a V_{OC} of 5.766 V and an FF of 71.2%) and low PCE retention (73.6%) observed in the control samples (Fig. 1f, g, Supplementary Table 15 and Table 1). Moreover, the PCE of various green-printed organic photovoltaics across different area scales are summarized in Fig. 1h and Supplementary Table 16 to further validate the feasibility of preparing high-performance modules by using rheology modifier strategies. The results after comparison show that these FDDO-optimized OSCs modules achieved one of the highest efficiencies and PCE retentions reported to date.

To address the critical issue of non-uniform morphology in green-printed active layer films, it is essential to provide a comprehensive

explanation of the movement and the spatial stacking situation of internal solutes based on fluid dynamics. Figure 2a displays the forces, gradients, and hydrodynamic phenomena during the printing process without/with the rheology modifier FDDO. Primarily, the distribution of solutes and molecular packing in the confined region are affected and subject to various forces, mainly including shear force (F_S), capillary force (F_C) driving capillary flow, and self-driving force (F_L) from Laplace pressure. The shear force generated by the blade shearing active layer solution influences the boundary-driven Couette flow within the solution, driving the solution to spread into a wet film[28]. And small molecules and polymers align and aggregate in response to the shear flow. Besides, the capillary force towards edge is induced by the significant evaporation rate difference between the evaporation three-phase contact line and the bulk solution. And the resulting capillary flow drives internal solutes to move and deposit at the periphery, leading to non-uniform solute deposition[29,32]. The movement and deposition of small molecule materials along the capillary flow towards the three-phase line is the main cause of CRE.

In addition, the actual printed gas/liquid interface parameters, including curvature and cross-section shape, are influenced and maintained by the Laplace pressure gradient resulting from the disparity in surface tension between the solution and the atmosphere[53]. Laplace pressure gradient plays an important role in the directed motion of liquid droplets, which has significant application value in fields such as fog water collection, microfluidics, and self-cleaning[37,38,41,43]. Moreover, it also performs an effective function in the self-assembly of nanostructures on curved surfaces and the directional transport of liquids[42,54]. The corresponding equation is presented in Eq. (1):

$$\Delta P(x) = P_{air} - P(x) = \sigma \cdot k(x) \tag{1}$$

Where $\Delta P(x)$ represents the Laplace pressure gradient at air/liquid interface, $P(x)$ is the Laplace pressure at position x in the gas/liquid confined interface, P_{air} is the pressure of air, σ is the surface tension of a droplet of liquid in air at the printing temperature, and $k(x)$ denotes the curvature of interface at position x. Also, the printing process gives rise to a Laplace pressure gradient within the solution, which is dependent on the shape and opening direction of the left and right interfaces. And the formula describing the Laplace pressure gradient within the gas/liquid confined zone during printing is presented in Eq. (2):

$$F_L \propto (P_R - P_L) = \sigma\left[k_L - k_R\right] \tag{2}$$

Where F_L denotes the self-driving force induced by the Laplace pressure gradient within the solution. P_R and P_L represent the mean values of Laplace pressure at the evaporation interface and the left interface in gas/liquid confined zone, respectively. And k_R and k_L are the corresponding mean curvatures of these interfaces. Based on this, by modulating the appropriate shape of the gas/liquid interface, it facilitates the construction of a suitable F_L within the solution against capillary force to uniform the solute distribution. To sum up, the resultant total driving force F_P that counteracts capillary force F_C and mitigates disordered particle stacking during the printing process is influenced and regulated by the shear force F_S, and the self-driving force F_L driven by the Laplace pressure gradient. The implementation of an appropriate F_P enables the high-throughput printing of high-quality large-area films.

To validate the efficiency of FDDO in homogenized films, the high-speed camera is employed to record the entire printing process of the active layer solution, both before and after optimization with FDDO, on 5 cm×5 cm PEDOT:PSS substrates (Fig. 2b, c). After optimization with FDDO, the contact angles at the left and right (evaporation) three-phase contact lines are significantly reduced from 63.1° and 23.6° to 49.6° and 16.8°, respectively. More importantly, a qualitative analysis of the curvature at the gas/liquid confined interfaces on both sides during blade-coating can be obtained from the results. The macroscopic confined zone stability is governed by the whole interfacial curvature, distinguishing it from the three-phase line contact angle which solely dictates local curvature. In the control solutions, the curvature on the left side of the gas/liquid confined interfaces is bigger than that on the right side, and both are concave interfaces. This result indicates that the atmospheric pressure is higher than the solution pressure at the right interface, which in turn is higher than the solution pressure at the left interface, thus creating a net driving force from right to left. The disparity between the curvature at the left interface and that of the evaporation interface indicates little Laplace pressure gradient across the solution. And the resultant driving force cannot completely offset the disordered aggregation of donor/acceptor pairs. After optimization, owing to the surfactant properties of FDDO, the discrepancy in curvature between the two sides increases, leading to a stronger intrinsic driving force, which facilitate a relatively homogeneous distribution of solutes during printing. Moreover, as shown in Fig. 2d, e, the contact angle of the FDDO-optimized active layer solution on the PEDOT:PSS substrate is 7.7°, which is lower than the 10.0° of the control samples. The smaller contact angle indicates that the FDDO-optimized solution spreads more extensively and can form a more uniform and controllable film.

Furthermore, to quantify the self-driving force induced by the internal Laplace pressure gradient, the ImageJ software is used to measure the curvatures of both interfaces (Fig. 2f–h and Supplementary Table 17). Additionally, the surface tension of the active layer solution and the viscosity of the processing solvent at the printing temperature are tested (Supplementary Figs. 26 and 27). To reduce the variability in the results, the mean curvature for the calculation is adopted. The difference in curvature between the left and right interfaces after FDDO optimization is 0.069 μm^{-1}, which is significantly higher than that of the reference sample (0.014 μm^{-1}). Moreover, the surface tension of the FDDO-optimized active layer solution decreased from 24.71 mN/m to 24.08 mN/m, deriving from the surfactant properties of FDDO. Besides, the viscosity is only slightly increased from 0.413 mPa·s to 0.419 mPa·s after adding a small amount of FDDO (3 wt %) into o-XY solvent, no significant viscosity change is observed. And the corresponding calculated value of F_L for the FDDO-optimized solution is approximately 4.8x that of the reference sample according to Eq. (2). Therefore, the FDDO-optimized solution has an intense Laplace pressure gradient in the same direction as the blade movement, resulting in more significant weakening of the capillary force. Small molecules moving toward the three-phase line with the capillary flow are more effectively inhibited. Consequently, the increase in Laplace pressure gradient reduces CRE, leading to a uniform active layer morphology. The higher F_L can reduce the disordered stacking of molecules and promote the homogeneous printing of the films. Additionally, the blade-substrate angle influences the interfacial shape in the gas-liquid confined region. To verify the reliability of results, FDDO-optimized active layer solutions are printed on full-ITO substrates under gradient blade-substrate angles (Supplementary Fig. 28). And the changes in interfacial curvatures during blade-coating process are statistically analyzed (Supplementary Fig. 29 and Supplementary Table 18). The results show that the Laplace pressure gradient at the corresponding gas/liquid confined zone is largest when the contact angle is almost 25°, consistent with the earlier results on device performance.

The phenomenon of high uniformity shown in digital photographs and the corresponding high performance of associated modules have been integrated with both qualitative theoretical analysis and quantitative computational results. The effect of the enhanced Laplace pressure gradient is effective in suppressing the CRE, thus eliminating the performance loss during the organic photovoltaic area expansion.

https://doi.org/10.1038/s41467-025-63530-y

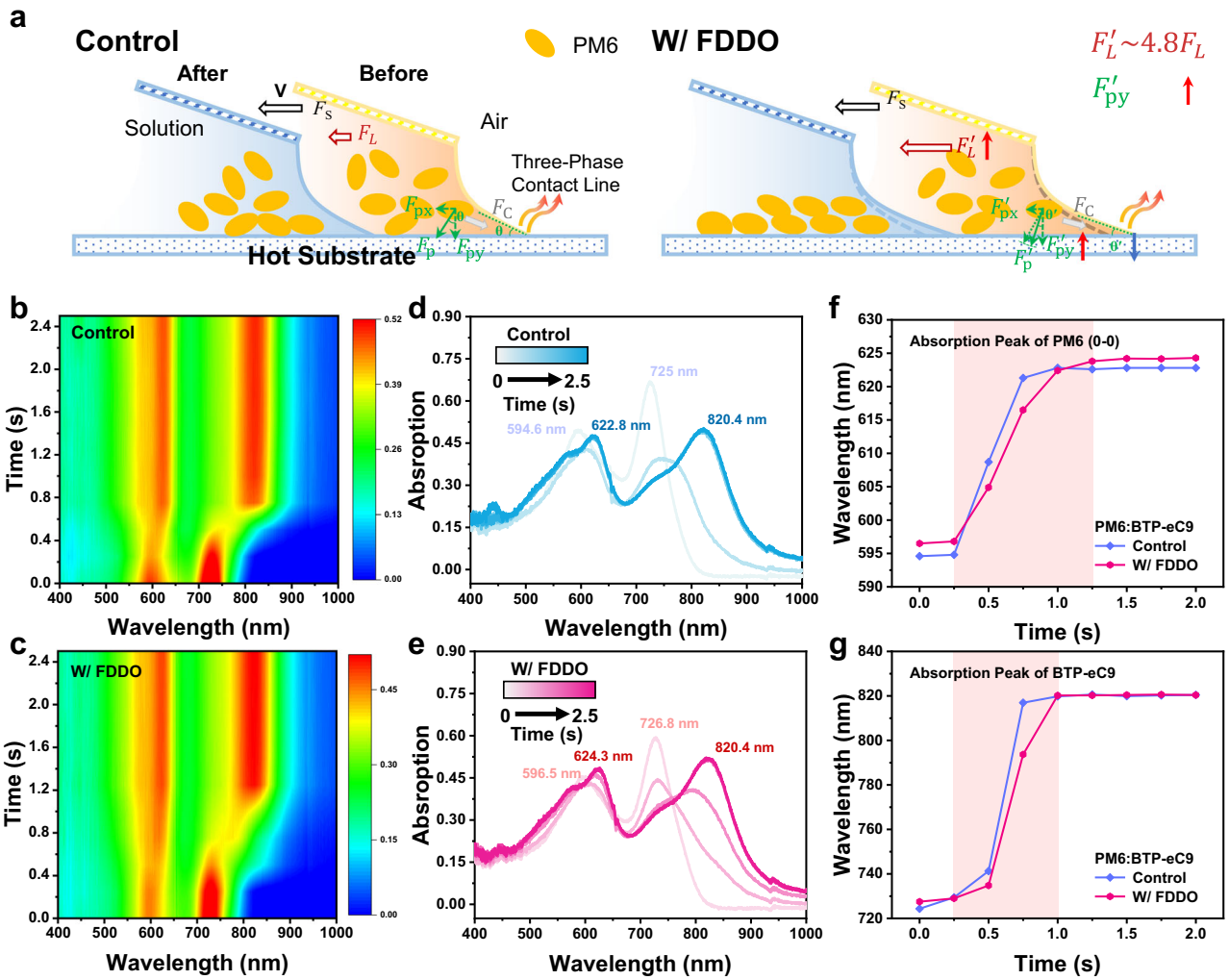

Fig. 3 | Schematic diagram of forces on polymer PM6 during printing and analysis of film formation kinetics. a Force analysis and crystalline stacking behavior of polymer PM6 during blade-coating process. Where F_S represents the shear force from machine settings. F_P represents the internal push force on the large-diameter polymer PM6 due to the edge of the gas/liquid confined interface of the wedge structure. And F_L originates from the in-solution Laplace pressure gradient. **b**, **c** Time evolution of UV-vis absorption spectra without/with FDDO during the blade-coating process. **d**, **e** Time evolution of UV−vis absorption line profiles without/with FDDO during the blade-coating process. **f** The peak position evolution as a function of time of PM6 in films without/with FDDO during the blade-coating process. **g** The peak position evolution as a function of time of BTP-eC9 in films without/with FDDO during the blade-coating process. Source data are provided as a Source Data file.

Simultaneously, to explore the corresponding crystallization and stacking behaviors during actual printing, the various forces on the polymer PM6 at printing gas/liquid confined zone are specifically analyzed and demonstrated in Fig. 3a. In contrast to the small molecule BTP-eC9, which can easily flow and deposit under the influence of various fluid dynamics such as capillary flow, the large-diameter polymer PM6 is more resistant to extensive movement under the same flow conditions. During the actual blade-coating process, the polymer PM6 molecules at the gas/liquid confined zone especially at evaporation three-phase contact line experience a series of forces. These mainly include shear force F_S, capillary force F_C, self-driving force F_L from Laplace pressure within the solution, and interfacial driving force F_P. These forces collectively act on the gas/liquid confined zone, influencing the crystallization behavior and molecular packing of PM6. Combining qualitative and quantitative analyses of high-speed camera results, F_L within the FDDO-optimized active layer solution is equivalent to 4.8 times that of the control solution. This enhanced F_L effectively suppresses the movement and deposition of the active layer solutes towards the three-phase line, leading to a more homogeneous distribution of the solutes. Further qualitative analysis revealed the changes in the F_P experienced by the polymer PM6 at the wedge-shaped evaporated three-phase contact line following FDDO optimization. More obviously, the optimal active layer solution has a smaller contact angle θ in the gas/liquid confined zone and a flatter curvature of the wedge-shaped three-phase line of evaporation. This leads to a larger F_{PY}, which favors the promotion of the directional alignment of polymer PM6 during the printing process. The optimal active layer solution has a smaller contact angle θ in the gas/liquid confined zone and a flatter curvature of the wedge-shaped evaporation three-phase line, allowing the PM6 to be subjected to greater forces. Accordingly, the polymer materials in the FDDO-optimized solution are subjected to a strong vertical component of force, thus enhancing their crystallinity. Based on the test results and forces analysis, the incorporation of FDDO can order the stacking behavior of PM6, enhance the crystallization of the active layer, ultimately homogenize the component distribution and film-forming quality of the active layer films.

To gain deeper insights into the critical details of how the rheology modifier FDDO influences the nucleation and film formation kinetics of the blend film during the blade-coating process, in-situ ultraviolet-visible (UV-vis) spectrophotometer is employed. Figure 3b,

https://doi.org/10.1038/s41467-025-63530-y

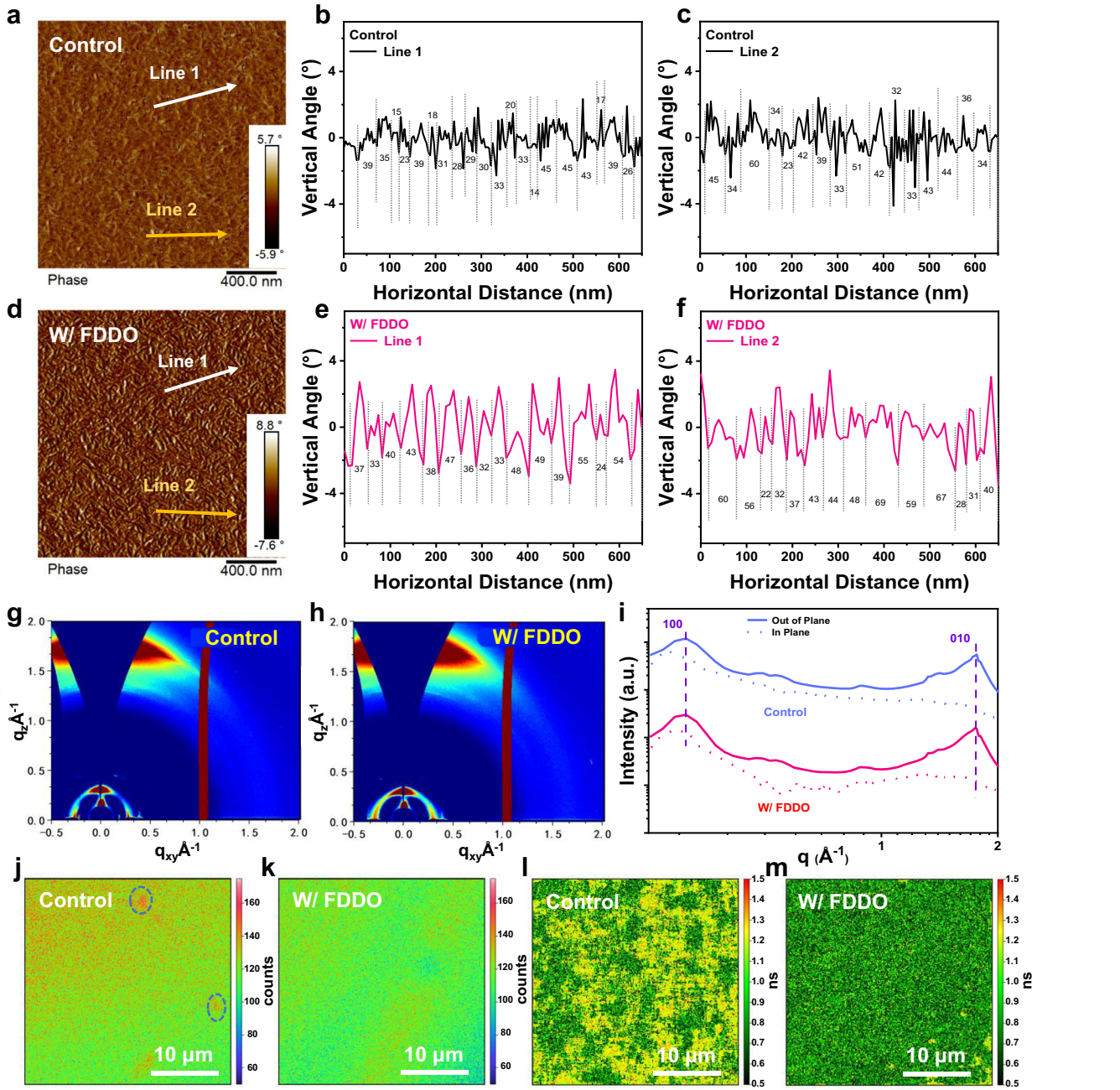

Fig. 4 | Analysis of the morphology and crystallization of printed active layers. **a**–**c** AFM phase image and fiber size distributions of PM6:BTP-eC9 blend films treated without FDDO. **d**–**f** AFM phase image and fiber size distributions of PM6:BTP-eC9 blend films treated with FDDO. **g**, **h** 2D GIWAXS patterns of the active layer films treated without/with FDDO. **i** 1D GIWAXS lines profiles of the corresponding blend films treated without/with FDDO. 2D PL **j**, **k** intensity and **l**, **m** lifetime distribution images of PM6:BTP-eC9 blend films treated without/with FDDO. Source data are provided as a Source Data file.

c presents the 2D time-resolved absorption spectra of the active layer films fabricated with o-XY and o-XY:FDDO, respectively. The results show a clear increase in the phase transition time and the absorption intensity of the donor and acceptor of the FDDO-modified active layer, which is beneficial to obtain high-purity phases and proper phase separation morphology. Moreover, the corresponding 1D absorption line profiles are demonstrated in Fig. 3d, e. Although the final PM6 absorption peak of the FDDO-modulated film is only red-shifted by about 1.5 nm compared to the control sample, the intensity of the BTP-eC9/PM6 peak in the final film increased, both reflecting an enhanced phase purity. And Fig. 3f, g illustrates the evolution of the absorption peak positions for both types of films at representative time points. Clearly, the film formation process can be divided into three distinct stages: an initial solution state characterized by a slow redshift in the absorption peak position as the solvent evaporates, a rapid film formation state marked by a swift redshift, and a final stable film state. In all three phases, the absorption peak positions of PM6 and acceptor (BTP-eC9) changed significantly. In the control samples, initially, the PM6 absorption peak stabilizes around 594.6 nm, and the intensity of this peak decreases and then increases, with a drastic redshift from 594.6 nm to about 623 nm, and finally stabilizes at about 623 nm. Compared to the control blend films, the FDDO-based blend films exhibit a longer phase transition time (1.00 s) than the standard sample (0.75 s) and red-shifted PM6 peak position. This extended phase

transition time is primarily attributed to the ability of FDDO to homogenize the dissolution and dispersion states of PM6 and the acceptor, while simultaneously restricting small molecular mobility through the perspective of fluid dynamics. This process facilitates the formation of more uniform phase separation and a more ordered molecular stacking microstructure, while simultaneously making the morphology of large-area printed active layers more controllable. Also, the UV-vis absorption spectroscopy of pure films shows enhanced crystallinity of both PM6 and BTP-eC9, in agreement with the in-situ UV-vis results (Supplementary Fig. 30).

To further validate the role of the rheology modifier FDDO on the morphology evolution in printing, the presence exploration of FDDO in the dried active layer films are specifically explored by means of X-ray photoelectron spectroscopy (XPS) and Fourier transform infrared spectroscopy (FT-IR) tests (Supplementary Figs. 31, 32). In previous studies, surfactants generally inhibited CRE by regulating surface tension to form inward Marangoni flow or by interacting with particles through electrostatic interactions[32,39,55]. Supplementary Fig. 31. shows the XPS test results of PM6:BTP-eC9 films processed with different ratio of FDDO. The original peak shifts of the PM6:BTP-eC9 films with moderate (3 wt%) and excessive (10 wt%) FDDO addition after alcohol elution do not change compared with the control film and no new peak appear. Therefore, there is no interaction between the FDDO and the photovoltaic materials in active layer. To further verify that the FDDO is eluted cleanly in the films, the FT-IR spectra of FDDO and PM6:BTP-eC9 (without FDDO addition, with 3 wt% FDDO addition and with 10 wt% FDDO addition) in solution and film states are displayed in Supplementary Fig. 32. In the FT-IR spectra of the FDDO solutions, a broad and strong vibrational peak located at 3285 cm^{-1} is observed, which corresponds to the stretching vibration of the hydroxyl groups (−OH) on both sides of FDDO. More importantly, two vibrational peaks appeared at 1144 and 1200 cm^{-1}, representing o-XY solvent-constrained $-CH_2-OH$ in-plane rocking and proximal $-CF_2-$ symmetric telescoping, respectively. After the incorporation of 3 wt% and 10 wt% FDDO into the PM6:BTP-eC9 solution, the vibrational peaks located at 1144 and 1200 cm^{-1} are continuously enhanced, indicating that FDDO is successfully introduced. While in the FT-IR spectra of the FDDO dried film, two peaks appeared at 1124 and 1253 cm^{-1}, representing $-CF_2-$ chain symmetric stretching and C–C coupling vibration, and terminal $-CF_2-$ asymmetric stretching vibration, respectively. After washing with alcohol, the corresponding characteristic peaks disappeared in the FDDO-incorporated PM6:BTP-eC9 films, while the peak shifts and intensities remained unchanged in the films with different FDDO additions, confirming the complete removal of FDDO in the dry films. This elution removal behavior aiming at FDDO arises from the synergistic combination of thermodynamically driven surface segregation during film deposition and high ethanol affinity. In short, the result indicates that there is no molecular interaction but pure rheological modulation between FDDO and the active layer components, confirming the reliability of the removal by alcohol elution, which differs from the previously reported surfactant selection and mechanism of action.

To investigate the positive effects of fluid control on the active layer morphology during the blade-coating process, atomic force microscopy (AFM) and transmission electron microscopy (TEM) are adopted. The AFM images of printed pure films and blend films, both un- and treated with FDDO, are demonstrated in Supplementary Figs. 33–37. After FDDO optimization, the crystallinity of pure PM6 and BTP-eC9 films is enhanced, and the fibrillated network morphology of PM6 is more pronounced, corroborating the conclusions of the previous enhanced forces analysis of polymer PM6. In comparison to the control film with excessive phase aggregation morphology (1.24 nm), the blend film based on PM6:BTP-eC9 with 3 wt% FDDO exhibits a more pronounced fibrous structure and shows stronger crystalline behavior (1.56 nm). Upon rising the FDDO content to 10 wt%, the roughness of active layer film also increased (1.63 nm). Afterwards, the profiles and distributions of cross-sectional fiber sizes along the arrow direction in the AFM phase images are extracted and analyzed (Fig. 4a–f and Supplementary Figs. 36–38). More importantly, the blend films optimized with FDDO display larger and more even fibril sizes (42 nm) than those of the control films (34 nm), primarily due to the optimized restricted behavior of interfacial edge, which can enhance the orientation of polymer PM6. This behavior is consistent with previous in-situ UV-vis spectra of blend films, favoring the reduced trap-assisted recombination and enhanced charge transport. The TEM images of printed active layer films, both un- and treated with FDDO, are demonstrated in Supplementary Fig. 39. Similarly, the TEM results demonstrated that the phase separation of the FDDO-optimized blended films is more pronounced. Moreover, the effect of FDDO on the surface energy of pure film is investigated by contact angle test (Supplementary Fig. 40). And the Flory-Huggins interaction parameter (χ) is calculated from the surface energy of films to explore the miscibility between the photovoltaic materials (Supplementary Table 19). After FDDO optimization, the surface energy of PM6 and BTP-eC9 pure films decreased from 31.47 mN/m and 39.27 mN/m to 29.22 mN/m and 38.46 mN/m, respectively, demonstrating the rheological modulation effect of FDDO. The χ value of the blend film treated by o-XY:FDDO ($\chi = 0.634$) is higher than that of the film treated by o-XY ($\chi = 0.431$), which favored the enhanced phase separation and high-purity phase domain formation of PM6 and BTP-eC9.

In order to deepen the understanding of the molecular stacking, phase separation and crystallization behaviors of the active layer films under different treatment conditions, the grazing incidence wide angle x-ray scattering (GIWAXS) and grazing incidence small angle X-ray diffraction (GISAXS) techniques are employed. Supplementary Fig. 41 and Fig. 4g–i show 2D and 1D GIWAXS images of pure PM6 and blend films treated without/with FDDO, respectively. And the relevant parameters of the (010) scattering peak in out-of-plane (OOP) direction are summarized in Supplementary Tables 20 and 21. The GIWAXS results for pure films indicates that FDDO suppresses the edge-on stacking of PM6 and optimizes the crystal orientation (Supplementary Fig. 41). For blend films, the o-XY:FDDO-treated film displays a more intense (010) π−π stacking peak at $q \approx 1.74$ $Å^{-1}$ in OOP direction, indicating a more pronounced face-on orientation in the film. The crystalline coherence lengths (CCL) of the blend films, extracted from the (010) diffraction peak in OOP direction, are 29.45 Å and 50.94 Å for the o-XY- and o-XY:FDDO-optimized films, respectively. The greater CCL value of the o-XY:FDDO-treated films indicate the tightest molecular stacking and strongest crystallinity, facilitating effective charge carrier separation and transport. In addition, the 2D and 1D GISAXS images of the blend films treated by o-XY and o-XY:FDDO are shown in Supplementary Fig. 42. And the corresponding parameters are displayed in Supplementary Table 22. The coherence length (ξ) represents the domain size of the donor-rich PM6 phase, while η and $2R_g$ correspond to the coherence length and crystallite size of the acceptor BTP-eC9, respectively. Upon optimal amount of FDDO incorporation, the ξ and $2R_g$ values of the active layer film increase from 22.9 nm and 13.4 nm to 25.6 nm and 15.2 nm, respectively, representing the enhanced phase separation and crystallinity. The introduction of FDDO is directly confirmed by GIWAXS and GISAXS characterizations, resulting in an active layer morphology with high crystallinity, high purity molecular phase domains and improved phase separation. The results are consistent with the AFM morphology of FDDO-optimized blended films with enhanced fibrillated interpenetrating networks.

The time-resolved confocal imaging system (TRCIS) is employed to assess the homogeneity and investigate the internal carrier dynamics of active layer films. The 2D PL images of the blend films without/with FDDO optimization under 523 nm laser excitation are shown in Fig. 4j, k and Supplementary Fig. 43a. Compared to the control films, the active layer films optimized by FDDO exhibit a

https://doi.org/10.1038/s41467-025-63530-y

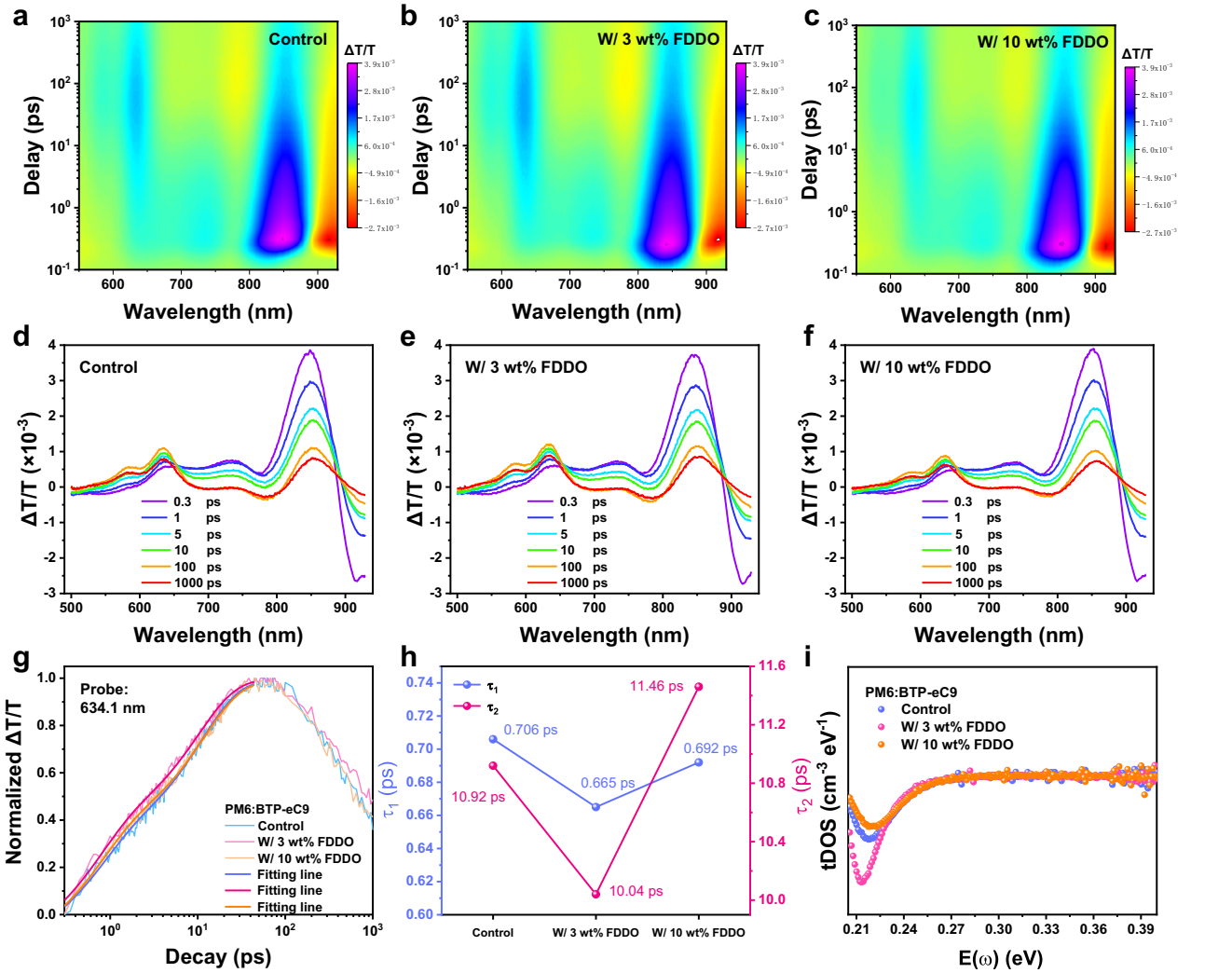

Fig. 5 | The kinetics of the exciton diffusion and hole transfer process. a–c 2D transient absorption spectra of the PM6:BTP-eC9 films processed by o-XY with 0 wt%, 3 wt%, 10 wt% of FDDO. **d–f** 1D transient absorption spectra of the PM6:BTP-eC9 films processed by o-XY with 0 wt%, 3 wt%, 10 wt% of FDDO. **g** Kinetic traces probing at 634.1 nm for PM6:BTP-eC9 films processed by o-XY with 0 wt%, 3 wt%, 10 wt% of FDDO. **h** Comparisons of τ_1 and τ_2 of different blend films. **i** Trap density of states (tDOS) spectra of PM6:BTP-eC9 devices processed by o-XY with 0 wt%, 3 wt%, 10 wt% of FDDO. Source data are provided as a Source Data file.

weaker PL intensity, which suggests a more efficient dissociation of electron-hole pairs into free carriers upon photoexcitation. Furthermore, the control blend films demonstrate more pronounced spatial PL intensity variations, attributed to non-uniform material deposition, including disordered molecular aggregation and defects. Figure 4l, m and Supplementary Fig. 43b and illustrates the corresponding 2D fluorescence lifetime images, and the specific lifetime distributions are placed in Supplementary Fig. 44. Clearly, compared to the original blend films, the lifetime images of the FDDO-optimized active layer film are more homogeneous and focused in distribution, in accordance with the fluorescence intensity results. In addition, the moderate FDDO-optimized active layer films exhibit a shorter average exciton lifetime (0.78 ns) compared to the original films (1.09 ns) and excessive FDDO-treated films (0.93 ns). This phenomenon can be ascribed to the fact that fluidic modulation optimizes the distribution of photovoltaic materials and reduces the defects and trap sites in blend films.

Additionally, the effect of FDDO treatment on the exciton and polariton dynamics of large-area (25 cm^2) blend films is investigated by using transient absorption spectroscopy (TAS)[56,57]. The transient absorption data recorded for the blend films based on PM6:BTP-eC9 system with no FDDO (control, 0 wt%), moderate FDDO (3 wt%), and excessive FDDO (10 wt%) under excitation at 800 nm are shown in Fig. 5a–f. And the kinetic data for the increase in the intensity of the ground state bleaching (GSB) peak at 634.1 nm are extracted and fitted by a double exponential function to estimate the characteristic time constants τ_1 and τ_2 (Fig. 5g, h), where τ_1 represents the dissociation time of the exciton at the donor/acceptor interface, τ_2 denotes the duration of exciton diffusion into the interface. The study demonstrates that the active layer film optimized with moderate amount of FDDO has the smallest values of both τ_1 (0.665 ps) and τ_2 (10.04 ps), when compared to the control film (a τ_1 of 0.706 ps and a τ_2 of 10.92 ps) and excessive FDDO-treated blend film (a τ_1 of 0.692 ps and a τ_2 of 11.46 ps). This indicates that the exciton separation and carrier transport processes are enhanced after the incorporation of 3% FDDO, benefiting from the clear fiber network morphology obtained by the proper fluid modulation effect of FDDO. Subsequently, the trap density of states (tDOS) of the devices are evaluated by thermal admittance spectroscopy (Fig. 5i). The tDOS of the FDDO-optimized device is reduced, which is consistency with the results of TAS, favoring the performance of the devices. Besides, the photoluminescence (PL) spectroscopy is recorded under excitation at 580 nm to study the performance discrepancies in exciton dissociation and charge

transport (Supplementary Fig. 45a). After FDDO optimization, the more efficient charge transfer in the blend film is found, indicating that the most efficient charge transfer occurs between donor/acceptor. And the transient fluorescence (TRPL) spectral curves are displayed in Supplementary Fig. 45b. As compared to the control film (89.8 ps) and the film treated by 10 wt% FDDO (105.4 ps), the lowest exciton lifetime (69.3 ps) is obtained in the film optimized by 3 wt% FDDO, indicating that the optimized films produced the highest photo-induced charge. Supplementary Fig. 46 shows the dark *J*–*V* curves of PM6:BTP-eC9-based devices treated with different concentration of FDDO. The results show that the device treated by 3 wt% FDDO has lower leakage current under reverse bias voltage and smaller series resistance (R_S) under positive bias voltage, in favor of improving J_{SC}, FF and PCE. Then, the Nyquist plots of electrochemical impedance spectra (EIS) of the devices treated with different concentrations of FDDO are measured (Supplementary Fig. 47). Experimental results exhibit that the charge transfer resistance (R_{ct}) of the 3 wt% FDDO-optimized devices is significantly reduced, illustrating fewer defects in the active layer film, which effectively improved the charge transfer efficiency. And the exciton dissociation and charge extraction behavior of device optimized by 3 wt% FDDO is more effective in saturation photocurrent test (Supplementary Fig. 48). In addition, the charge recombination behavior in the devices is further explored by studying the relationship between J_{SC}, V_{OC} and light intensity (Supplementary Fig. 49). The results show that the FDDO-optimized devices exhibit the slightest bimolecular recombination and trap-assisted recombination, attributing to the reduced defect density of the printed films by the rheology modulation strategy. Subsequently, the carrier lifetime (τ_{rec}) and charge extraction time (τ) of the devices treated with different concentrations of FDDO are characterized by using transient photovoltage (TPV) and transient photocurrent (TPC) techniques. The devices optimized by 3 wt% FDDO have faster charge extraction time (τ = 0.39 μs) and longer carrier lifetime (τ_{rec} = 272.8 μs) among them (Supplementary Fig. 50). Thus, the space charge-limited current (SCLC) test shows that the 3 wt% FDDO-optimized devices have higher hole mobility (μ_h) and electron mobility (μ_e). And the ratio of hole mobility to electron mobility (μ_h/μ_e) is closer to 1 for the 3 wt% FDDO-optimized devices, demonstrating more efficient and balanced carrier transport behaviors (Supplementary Fig. 51). Based on the above test results, the incorporation of FDDO can improve the exciton dissociation and carrier transport behaviors in the OSCs, thus corroborating the improved photovoltaic performance of the devices.

Stability stands as a key factor in assessing the industrialization potential of photovoltaic technology. Significantly, the fluidic modulation ability of the rheology modifier FDDO combined with the alcohol elution property also contributed to the device stability. Enhanced polymer crystallization and weakened CRE both improve device stability. First, unencapsulated devices are subjected to continuous heating at 85 °C in the N_2-filled atmosphere to investigate the effect of thermal aging environment on device performance (Supplementary Fig. 52a). After 50 days of aging, the PCE of control devices decay to 72.2% of the original value, while the FDDO-optimized devices still maintain 81.9% of the initial value, benefiting from the optimized film morphology obtained through the fluid modulation effect of FDDO in blade-coating process. Moreover, the encapsulated devices are continuously heating at 85 °C/85% RH to test the damp heat stability (Supplementary Fig. 52b). The control devices experienced a rapid degradation with an almost 80% drop in initial efficiency after 20 days. By contrast, the FDDO-treated device maintains an initial efficiency of 59.9%. Supplementary Fig. 53 demonstrates the variation of PCE of unencapsulated devices with the maximum power point (MPP) tracking test time under nitrogen environment at 25 °C. After optimization, the T_{90} and T_{80} lifetimes of the PM6:BTP-eC9-based devices are significantly improved, from 84 h and 282 h to 401 h and 986 h, respectively.

Discussion

In conclusion, we obtain large-area uniform films with enhanced face-on orientation and high crystallinity by doping the rheology modifier FDDO to optimize the fluid behavior within the active layer solution during blade-coating process. From the perspective of printed fluid mechanics, the FDDO-optimized solution exhibits a 4.8-fold increase in the Laplace pressure gradient along the printing direction compared to control solution, which directly suppresses the movement of solutes towards the edges. The reduction in small molecules moving toward the three-phase line is conducive to CRE inhibition. Moreover, the enhanced internal driving force within the solution and intensive vertical component force in the printed FDDO-optimized gas/liquid confined zone promote polymer crystallization. The introduction of FDDO leads to enhanced crystallinity and face-on orientation of PM6, which facilitates the formation of high-purity crystalline phases and proper phase separation, thus promoting exciton dissociation and charge transport. Therefore, the effects of the Laplace pressure gradient effectively inhibit the inhomogeneous distribution of active layer components, which facilitates the preparation of high-quality, large-area active layer films. Furthermore, based on the PM6:BTP-eC9 system, when the device area is expanded from 0.04 cm^2 to 16.94 cm^2, the PCE of the OSCs decreased from 18.66% to 16.55%, demonstrating a high PCE retention rate of 88.7%. In addition, the successful application in the PM6:BTP-eC9:L8-BO system validates the universality of this strategy. FDDO-optimized small-area (0.04 cm^2), large-area (1 cm^2) devices and modules (25 cm^2) achieve advanced PCEs of 20.49%, 19.32% and 17.85%, respectively. Since FDDO has no interaction with the photovoltaic materials in active layer and can be completely eluted by ethanol, it performs well in many different active layer solutions. The universality of FDDO has also been verified through its successful application in various systems. Under MPP testing conditions, the FDDO-optimized device exhibits great photostability, achieving a T_{80} of 986 h. Simultaneously, the device maintains nearly 60% of its initial efficiency after 20 days of continuous aging at 85 °C and 85 RH%. The proposed strategy aims to improve the film homogeneity of active layer by modulating the rheological behavior during the printing process. This approach is expected to expand the processing window for industrial production of large-area organic photovoltaics.

Methods

Materials

PM6, BTP-eC9, L8-BO, IT-4F, PTQ10 and PDINN are purchased from Solarmer Materials Inc. Indium-tin oxide (ITO) glass is gained from South China Science & Technology Company Limited, whereas PEDOT:PSS (Clevios P VP AI4083) is obtained from Heraeus. o-Xylene (o-XY), Carbon disulfide (CS_2) and 2,2,3,3,4,4,5,5,6,6,7,7,8,8,9,9-Hexadecafluoro-1,10-decanediol (FDDO) are purchased from Macklin Reagent Inc. And Toluene is purchased from Xilong Scientific Co., Ltd. Ag is obtained from Zhong Nuo Advanced Material Technology Co., Ltd. Other chemicals and solvents are purchased from Sigma-Aldrich Co., Ltd. and used without further purification.

Devices fabrication

Organic solar cells are constructed on ITO glass substrates. The device structure comprise ITO/PEDOT:PSS (30 nm)/PM6:BTP-eC9 or PTQ10:BTP-eC9 or PM6:IT-4F or PM6:BTP-eC9:L8-BO/PDINN (10 nm)/Ag. The ITO-coated glass substrates are sequentially cleaned with deionized water, acetone and isopropyl alcohol using ultrasonication, then dried with N_2. Then, the substrates underwent a 20-min ultraviolet-ozone treatment. A PEDOT:PSS layer is spin-coated at 4000 rpm for 40 s onto the ITO substrates and annealed at 150 °C for 20 min in ambient atmosphere. Silicon wafer is treated with UVO for 10 min and then utilized as the blade. The active layers are blade-coated from o-XY solution with the optimal donor/acceptor weight ratios of 1:1.2 with a total

concentration of 17 mg mL^{-1}, with a thickness control of 110 nm. The rheology modifier FDDO is introduced approximately 45 min prior to the printing process, with an optimal concentration of 3 wt.% (MFDDO:-Mactive layer materials = 3%). The blade is moved at the speed of 45 mm s^{-1} in air with the RH of 30%-60%. After that, the active layer films are annealed by printing using hot ethanol solvent. The solutions are blade-coated onto the substances with areas of 2.25, 9, 16 and 25 cm^2 for small-area and large-area OSCs, respectively. And the effective areas of the corresponding OSCs devices or modules are 0.04, 1, 1.44, 3, 4 and 16.94 (2.42*7) cm^2. After that, active layer films are transferred to the N_2-filled glovebox. Then, PDINN is dissolved at the concentration of 1 mg mL^{-1} in methanol and coated at 3000 rpm (30 s). Finally, 100 nm Ag is deposited by vacuum evaporation under high vacuum (~5×10^{-4} Pa). The OSC modules are fabricated by successively etching the ITO, PDINN, and Ag layers with P1, P2, and P3 lines using a femtosecond laser to connect the subcells in series.

Optical characterizations

The current-voltage (*J*–*V*) characteristics are measured by a Keithley 2400 Source Meter in N_2-filled glovebox under simulated solar light (100 mW/cm^2, AM 1.5 G, Abet Solar Simulator Sun2000). The standard silicon solar cell is corrected from NREL and the currents are detected under the solar simulator. The effective area of devices is determined by the calibrated apertures (0.04 cm^2, 1.00 cm^2, 1.44 cm^2, 3.00 cm^2 and 4.00 cm^2). The scan range is from −0.2 V to 1.0 V, with a scan rate of 0.2 V/s, a delay time of 30 ms and the each step of 20 mV. The EQE spectra are recorded on a commercial EQE measurement system (Enlitech, QE-R3011) in N_2-filled glovebox. The UV-vis absorption spectra are recorded on a PerkinElmer Lambda 750 spectrophotometer. The steady state photoluminescence (PL) spectrum is achieved by a Shamrock sr-303i-B spectrometer from Andor Tech. PL spectra are excited by a Xe flash lamp. And the time-resolved photoluminescence (TRPL) is measured by using an Edinburgh Instruments FLS920 spectrometer.

OM, 3D microscopy, AFM, TEM and GIWAXS characterizations

Optical microscopy (OM) images are taken with a KCC-REM-HVZ-HRM-300 optical microscope at OM magnification of 50.0x. Three-dimensional (3D) microscopy images are obtained by ContourGT-K 3D microscope. Atomic force microscopy (AFM) images are measured by a MultiMode 8-HR (Bruker). Transmission electron microscopy (TEM) images are taken by a JEOL-2100F transmission electron microscope and an internal charge-coupled device (CCD) camera. The TEM films are fabricated with ITO/PEDOT/PSS/active layers, float on the water surface and collected on a copper mesh. The GIWAXS data are obtained at 1W1A Diffuse X-ray Scattering Station, Beijing Synchrotron Radiation Facility (BSRF-1W1A). Samples are prepared by blade-coating under device conditions on the Si substrates. The energy of incidence is 10 keV and the X-ray wavelength of the sample is 0.124 nm.

Surface energy characterization

The value of χ is computed from the equation:

$$\chi_{1,2} \propto \left(\sqrt{\gamma_1} - \sqrt{\gamma_2}\right)^2 \tag{3}$$

Where γ is the surface tension of samples. In addition, we test the surface tension of the solution of the active layer at printing temperature by using the hanging drop method, which is based on the Young-Laplace equation. The contact angle, surface tension, and surface free energy are performed at a Krüss DSA100s Drop Shape Analyzer.

Blade-coating machine

Large-area modules are prepared by desktop multi-functional and high-precision coating equipment (SSL-BCM-002, Nantong Rollshine Photoelectric Technology Co., Ltd.).

Space Charge Limited Current (SCLC) characterization

Electron and hole mobilities are measured by using the SCLC method. Electron-only (ITO/ZnO/active layer/PDINN/Ag) devices and hole-only (ITO/PEDOT:PSS/active layer/MoO_3/Ag) devices are fabricated. The mobilities are obtained by taking current-voltage curves and fitting the results to a space charge limited form, where the SCLC is described by:

$$J = 9\varepsilon_r\varepsilon_0\mu V^2/8L^3 \tag{4}$$

Where ε_0 is the permittivity of free space (8.854×10^{-12} F^{-1}m^{-1}), V is the difference of applied voltage (V_{app}) and offset voltage (V_{bi}), ε_r is the relative permittivity of the material (assumed to be 3), μ is the electron or hole mobility and L is the thickness of the film. From the plots of $J^{1/2}$ vs V, electron and hole mobilities can be deduced. The thickness of blend films is determined by a BRUKER DektakXT Surface Profilometer.

Transient absorption spectroscopy (TAS) characterization

For femtosecond transient absorption spectroscopy, the total output of the Yb:KGW laser (1030 nm, 220 fs Gaussian fit, 100 kHz; Light Conversion Ltd) is separated into two beams of light. One beam is brought to NOPA (ORPHEUS-N, Light Conversion Ltd). One beam is introduced to the NOPA (ORPHEUS-N from Light Conversion Ltd) to produce a specific wavelength for the pump beam (here, 800 nm is used). The other beam is focused onto a YAG plate to form a white light continuum probe beam. The pump and probe overlap at a slight angle of less than 10° on the sample. A linear CCD array collects the transmitted probe light from the sample. For all TA measurements, samples are kept in an N_2-filled cell at 25 °C. Subsequently, this equation is utilized to obtain a transient differential transmission signal:

$$\frac{\Delta T}{T} = \frac{T_{\text{pump-on}} - T_{\text{pump-off}}}{T_{\text{pump-off}}} \tag{5}$$

Devices stability tests

Maximum Power Point (MPP) testing is conducted in a nitrogen atmosphere at 25 °C. The light sources are calibrated against standard reference solar cells to ensure spectral accuracy. Moreover, the thermal stability at 85 °C are tested in a nitrogen atmosphere. To examine thermal and humidity stability, the device is placed in a dark environment with a temperature of 85 °C and a humidity of 85% relative humidity.

Reporting summary

Further information on research design is available in the Nature Portfolio Reporting Summary linked to this article.

Data availability

The data that support the findings of this study are available from the corresponding authors upon request. Source data are provided with this paper.

References

1. Wang, Z. et al. Self-sustaining personal all-day thermoregulatory clothing using only sunlight. *Science* **382**, 1291–1296 (2023).
2. Yu, G., Gao, J., Hummelen, J. C., Wudl, F. & Heeger, A. J. Polymer photovoltaic cells: Enhanced efficiencies via a network of internal donor-acceptor heterojunctions. *Science* **270**, 1789–1791 (1995).
3. Chen, D. et al. Printable and stable all-polymer solar cells based on non-conjugated polymer acceptors with excellent mechanical robustness. *Sci. China Chem.* **65**, 182–189 (2022).
4. Jiang, Y. et al. Non-fullerene acceptor with asymmetric structure and phenyl-substituted alkyl side chain for 20.2% efficiency organic solar cells. *Nat. Energy* **9**, 975–986 (2024).

5. Xiong, S. et al. Waterproof and ultraflexible organic photovoltaics with improved interface adhesion. *Nat. Commun.* **15**, 681 (2024).
6. Meng, X., Xing, Z., Hu, X. & Chen, Y. Large-area flexible organic solar cells: Printing technologies and modular design. *Chin. J. Polym. Sci.* **40**, 1522–1566 (2022).
7. Cheng, P., Li, G., Zhan, X. & Yang, Y. Next-generation organic photovoltaics based on non-fullerene acceptors. *Nat. Photonics* **12**, 131–142 (2018).
8. Wei, N. et al. Constructing multiscale fibrous morphology to achieve 20% efficiency organic solar cells by mixing high and low molecular weight D18. *Adv. Mater.* **36**, 2408934 (2024).
9. Guan, S. et al. Self-assembled interlayer enables high-performance organic photovoltaics with power conversion efficiency exceeding 20%. *Adv. Mater.* **36**, 2400342 (2024).
10. Sun, Y. et al. -Extended nonfullerene acceptor for compressed molecular packing in organic solar cells to achieve over 20% efficiency. *J. Am. Chem. Soc.* **146**, 12011–12019 (2024).
11. Song, J. et al. Non-halogenated solvent-processed organic solar cells with approaching 20% efficiency and improved photostability. *Angew. Chem. Int. Ed.* **63**, e202404297 (2024).
12. Wang, J. et al. Physical insights into non-fullerene organic photovoltaics. *Nat. Rev. Phys.* **6**, 365–381 (2024).
13. Wang, G., Adil, M. A., Zhang, J. & Wei, Z. Large-area organic solar cells: Material requirements, modular designs, and printing methods. *Adv. Mater.* **31**, 1805089 (2019).
14. Hu, X. T., Liu, S. Q., Song, Y. L. & Chen, Y. W. New thin-film solar cells: Flexible design and printing manufacturing. *Acta Polym. Sin.* **54**, 910–926 (2023).
15. Zhang, B. et al. Rapid solidification for green-solvent-processed large-area organic solar modules with >16% efficiency. *Energy Environ. Sci.* **17**, 2935–2944 (2024).
16. Xue, P., Cheng, P., Han, R. P. S. & Zhan, X. Printing fabrication of large-area non-fullerene organic solar cells. *Mater. Horiz.* **9**, 194–219 (2022).
17. Li, H. et al. Advances in the device design and printing technology for eco-friendly organic photovoltaics. *Energy Environ. Sci.* **16**, 76–88 (2023).
18. Lucera, L. et al. Guidelines for closing the efficiency gap between hero solar cells and roll-to-roll printed modules. *Energy Technol.* **3**, 373–384 (2015).
19. Zhao, H. et al. Hot hydrocarbon-solvent slot-die coating enables high-efficiency organic solar cells with temperature-dependent aggregation behavior. *Adv. Mater.* **32**, 2002302 (2020).
20. Su, Y. et al. High-efficiency organic solar cells processed from a halogen-free solvent system. *Sci. China Chem.* **66**, 2380–2388 (2023).
21. Xu, L. et al. Volatile solid-assisted molecular assembly enables eco-friendly processed organic photovoltaic cells with high efficiency and photostability. *Adv. Funct. Mater.* **34**, 2314178 (2024).
22. Sun, M. et al. Overcoming disordered preaggregation in liquid state for highly efficient organic solar cells printed from nonhalogenated solvents. *Adv. Energy Mater.* **13**, 2203465 (2023).
23. Jia, Z. et al. Eco-friendly volatile additive enabling efficient large-area organic photovoltaic module processed with non-halogenated solvent. *Energy Environ. Sci.* **17**, 3908–3916 (2024).
24. Cheng, J. et al. Device engineering of non-fullerene organic photovoltaics with extrapolated operational T80 lifetime over 45,000 h in air. *Joule* **8**, 2250–2264 (2024).
25. Cui, F. et al. Using an external electric field to tune active layer morphology enabling high-efficiency organic solar cells via ambient blade coating. *Sci. Adv.* **10**, eado5460 (2024).
26. Liu, S. et al. Pseudo-planar heterojunction organic photovoltaics with optimized light utilization for printable solar windows. *Adv. Mater.* **34**, 2201604 (2022).
27. Chen, H. et al. A guest-assisted molecular-organization approach for >17% efficiency organic solar cells using environmentally friendly solvents. *Nat. Energy* **6**, 1045–1053 (2021).
28. Wang, H. et al. Green printing for scalable organic photovoltaic modules by controlling the gradient Marangoni flow. *Adv. Mater.* **36**, 2313098 (2024).
29. Huang, C. et al. Meniscus-modulated blade coating enables high-quality α-phase formamidinium lead triiodide crystals and efficient perovskite minimodules. *Joule* **8**, 2539–2553 (2024).
30. Mousavi, S. M., Raveshiyan, S., Amini, Y. & Zadhoush, A. A critical review with emphasis on the rheological behavior and properties of polymer solutions and their role in membrane formation, morphology, and performance. *Adv. Colloid Interface Sci.* **319**, 102986 (2023).
31. Gu, X., Shaw, L., Gu, K., Toney, M. F. & Bao, Z. The meniscus-guided deposition of semiconducting polymers. *Nat. Commun.* **9**, 534 (2018).
32. Kim, H. et al. Controlled uniform coating from the interplay of Marangoni flows and surface-adsorbed macromolecules. *Phys. Rev. Lett.* **116**, 124501 (2016).
33. Mampallil, D. & Eral, H. B. A review on suppression and utilization of the coffee-ring effect. *Adv. Colloid Interface Sci.* **252**, 38–54 (2018).
34. Routh, A. F. Drying of thin colloidal films. *Rep. Prog. Phys.* **76**, 046603 (2013).
35. Weon, B. M. & Je, J. H. Capillary force repels coffee-ring effect. *Phys. Rev. E* **82**, 015305 (2010).
36. Roché, M. et al. Marangoni flow of soluble amphiphiles. *Phys. Rev. Lett.* **112**, 208302 (2014).
37. Yang, L. et al. Selective directional liquid transport on shoot surfaces of Crassula muscosa. *Science* **384**, 1344–1349 (2024).
38. Wang, Z. et al. Directional moisture-wicking triboelectric materials enabled by Laplace pressure differences. *Nano Lett.* **24**, 7125–7133 (2024).
39. Stetten, A. Z. et al. Surfactant-induced Marangoni transport of lipids and therapeutics within the lung. *Curr. Opin. Colloid .* **36**, 58–69 (2018).
40. Sun, Q. et al. Curved nanofiber network induces cellular bridge formation to promote stem cell mechanotransduction. *Adv. Sci.* **10**, 2204479 (2023).
41. Zheng, Y. et al. Directional water collection on wetted spider silk. *Nature* **463**, 640–643 (2010).
42. Li, X. et al. Continuous and controllable liquid transfer guided by a fibrous liquid bridge: Toward high-performance QLEDs. *Adv. Mater.* **31**, 1904610 (2019).
43. Zhang, K. et al. A strategy to drive nanoflow using Laplace pressure and the end effect. *Droplet* **3**, e136 (2024).
44. Gouveia, B. et al. Capillary forces generated by biomolecular condensates. *Nature* **609**, 255–264 (2022).
45. Kim, T., Kim, B. J., Bonacchini, G. E., Ostrovsky-Snider, N. A. & Omenetto, F. G. Silk fibroin as a surfactant for water-based nanofabrication. *Nat. Nanotechnol.* **19**, 1514–1520 (2024).
46. Oratis, A. T., Bush, J. W. M., Stone, H. A. & Bird, J. C. A new wrinkle on liquid sheets: Turning the mechanism of viscous bubble collapse upside down. *Science* **369**, 685–688 (2020).
47. Min, F., Dreiss, C. A. & Chu, Z. Dynamic covalent surfactants and their uses in the development of smart materials. *Adv. Colloid Interface Sci.* **327**, 103159 (2024).
48. Sethurajaperumal, A., Uppara, P. V. & Varrla, E. Low-temperature decomposable industrial surfactant for stabilization of few-layered graphene in water. *Carbon* **228**, 119375 (2024).
49. Luo, S. et al. Uniform spread of high-speed drops on superhydrophobic surface by live-oligomeric surfactant jamming. *Adv. Mater.* **31**, 201904475 (2019).

50. Zhang, M., Guo, X., Ma, W., Ade, H. & Hou, J. A large-bandgap conjugated polymer for versatile photovoltaic applications with high performance. *Adv. Mater.* **27**, 4655–4660 (2015).
51. Cui, Y. et al. Single-junction organic photovoltaic cells with approaching 18% efficiency. *Adv. Mater.* **32**, 1908205 (2020).
52. Li, C. et al. Non-fullerene acceptors with branched side chains and improved molecular packing to exceed 18% efficiency in organic solar cells. *Nat. Energy* **6**, 605–613 (2021).
53. Lu, H. et al. Active bacterial anti-adhesion strategy based on directional transportation of droplet self-actuated by Laplace pressure gradient on self-actuated and infrared sensing responsive platform. *Chem. Eng. J.* **475**, 146348 (2023).
54. Su, M. et al. Non-lithography hydrodynamic printing of micro/nanostructures on curved surfaces. *Angew. Chem. Int. Ed.* **59**, 14234–14240 (2020).
55. Anyfantakis, M., Geng, Z., Morel, M., Rudiuk, S. & Baigl, D. Modulation of the coffee-ring effect in particle/surfactant mixtures: the importance of particle-interface interactions. *Langmuir* **31**, 4113–4120 (2015).
56. Zhan, L. et al. Multiphase morphology with enhanced carrier lifetime via quaternary strategy enables high-efficiency, thick-Film, and large-area organic photovoltaics. *Adv. Mater.* **34**, 2206269 (2022).
57. Zhang, M. et al. Efficient and stable high-entropy organic photovoltaics. *Joule* **9**, 101851 (2025).

Acknowledgements

Y.C. thanks the National Natural Science Foundation of China (NSFC 52333006), National Key R&D Program of China: Strategic International Innovation Cooperation (2024YFE0209400). X.H. thanks the National Natural Science Foundation of China (NSFC 52222312, 22461142139, 52173169), Natural Science Foundation of Jiangxi Province (20242BAB24002, 20224ACB204007). S.L. thanks the National Natural Science Foundation of China (NSFC 52303316), the China Postdoctoral Science Foundation under Grant Number 2023M741484. This work was also carried out with the support of Shanghai Synchrotron Radiation Facility, BL02U2.

Author contributions

Y. Chen and X.H. conceived and designed the experiments. S.L. fabricated the OSCs and completed the writing of the manuscript. S.L. and H.W. measured the various photoelectric properties and film characterizations (UV-vis, PL, contact angles, etc.). Y. Cui and S.Z. tested the photographs based on high-speed camera. Ha. L. measured the AFM images. C.S. and L.Y. assisted in the GIWAXS measurements and analysis. Ho. L. analyzed and tested the GISAXS characterization. H.Y. tested the photographs based on three-dimensional camera. H.Z., J.Y. and H.C. tested and analyzed transient absorption spectroscopy.

Competing interests

The authors declare no competing interests.

Additional information

Supplementary information The online version contains supplementary material available at https://doi.org/10.1038/s41467-025-63530-y.

Correspondence and requests for materials should be addressed to Xiaotian Hu or Yiwang Chen.

Peer review information *Nature Communications* thanks Hyeok Kim, Kenjiro Fukuda, and the other, anonymous, reviewer(s) for their contribution to the peer review of this work. A peer review file is available.